SUPPLEMENTAL MATERIALS

S1. Conceptual replication in the INSIGHT-1b dataset

It is a growing concern that findings from the psychological and brain sciences fail to replicate. As such, we adopted a conceptual replication approach where the same predictions are tested, but through a variety of different means[1]. Our results align with core predictions from Network Neuroscience Theory (NNT), and the findings from the main text.

Here, participants were drawn from a sample of healthy adults from the INSIGHT study, a randomized controlled trial investigating the efficacy of multi-modal interventions for enhancing cognitive performance (for details, see refs.[2,3]). Previous research has demonstrated the appropriateness of this dataset for using brain topology to predict general intelligence. A study using the trial's first cohort found significant relations between functional topology and fluid intelligence[4]. A separate study focused on the trial's second cohort used functional topology to successfully predict general intelligence[5]. Sections S1-S7 reflect a joint modeling approach of structural topology and intrinsic functional coactivation patterns to investigate core predictions of NNT within the trial's second cohort (see main text for presentation of predictions).

S1.1. Participants and inclusion criteria

The inclusion criteria for the INSIGHT study were designed to ensure the sample is well-characterized given the hypotheses, capable of performing the tasks, and compatible with the machinery used. Thus, we included adults (1) aged 18-44 years; (2) fluent in English; (3) possessing at least a high-school diploma; (4) with normal or corrected to normal vision and hearing; (5) free of any psychoactive medication; (6) without history of neurological, psychological, or endocrine disease; (7) without history of concussion for the past 2 years; (8) not having learning disorders; (9) not smoking more than 10 cigarettes a day; (10) with a body mass index less than 35; (11) with at least one positive response on the revised Physical Activity Readiness Questionnaire[6]; and (12) right-handed.

Two hundred and forty-six subjects in the sample completed all cognitive tests and underwent all magnetic resonance imaging (MRI) scans (i.e., anatomical, diffusion-weighted, and resting state). We applied strict data quality criteria to choose a subset of subjects representing a well-characterized sample in line with the study's hypotheses. The seven intrinsic connectivity networks (ICNs) described by Yeo and colleagues[7] could be extracted from 182 individuals using an automatic extraction algorithm (see section S3.3 below for details). Given

the importance of ICNs for our hypotheses, we focused our analysis on this set of subjects with comprehensive network labeling. To ensure the reliability of our connectome-based predictive model (CPM), a strict motion threshold (≤ 0.15mm) was set for average framewise displacement (FD). Excluding subjects with significant motion in their data resulted in our final sample of 145 participants. Participants were aged 18-43 years (M = 23.39; SD = 4.9) and 53% were female.

Bias checks. We performed additional analyses to ensure that the subject selection process had not biased behavior-related results. An independent samples t-test comparing subjects that passed or failed the ICN extraction procedure did not show a difference in g scores (M_{passed} = -0.08; SD = -0.92; M_{failed} = -0.01; SD_{failed} = 0.77; $t(244)$ = -0.53; p = 0.60). This suggests that the ICN extraction process did not impact the relationship between the brain's topological organization and g observed in this study. In addition, the selection process did not undermine the normality of the g scores, as revealed by the Lilliefors normality test (D = 0.05; p = 0.50).

We investigated whether the comprehensive extraction of ICNs was affected by in-scanner motion (i.e., average framewise displacement). FD values were log-transformed to ensure normality. The Lilliefors normality test indicated log-transformed distributions of FD for the groups that passed or failed the ICN extraction procedure did not significantly differ from a normal distribution (D_{passed} = 0.99; p_{passed} = 0.54; D_{failed} = 0.10; p_{failed} = 0.14). We found that the passed group had a significantly lower average FD (M_{passed} = -2.20; SD_{passed} = 0.34) compared to the failed group (M_{failed} = -2.08; SD_{failed} = 0.40; $t(244)$ = -2.33; p = 0.02). This suggests that less motion is important for the extraction of all seven ICNs.

Finally, we examined whether motion, age and sex were significantly related with g. To test this, we correlated FD values and age with g, while fitting a logistic regression model to test the relationship between sex and g. Neither FD values (r = 0.04; t(143) = 0.48; p = 0.63), nor age (r = 0.02; t(143) = 0.24; p = 0.81) were significantly related to g. Sex also showed no significant association (β = 0.34; z = 1.73; p = 0.08).

S2 Derivation of *g*

S2.1. Cognitive battery

The INSIGHT study used a large battery of cognitive tests to derive a general factor of intelligence for each participant. These tests included: (1) the Law School Admissions Test Logical

Reasoning Battery[8]; (2) a figure series completion test of fluid intelligence[9]; (3) the Shipley-2 vocabulary test[10] as a measure of crystallized intelligence; and (4) the Adult Decision-Making Competency battery[11] (ADMC).

The choice of the cognitive battery is based on careful examination of various tests' psychometric properties, as well as providing coverage of major facets of general intelligence. The Law School Admissions Test of Logical Reasoning Battery was included as a measure of deductive reasoning ability, related to *g*[12]. The Figure Series Completion test provided a measure of fluid intelligence, while Shipley-2 vocabulary tests were used to evaluate crystallized intelligence (see ref.[13] for the importance of including both in measures of intelligence). The ADMC, a battery of decision-making competence measures, was employed based on prior work demonstrating strong associations between its subtests and canonical measures of general intelligence[14–16]. The subtests included from the ADMC were: (1) application of decision rules; (2) resistance to framing; (3) consistency in risk perception; (4) recognizing social norms; and (5) resistance to sunken costs.

S.2.2. Factor analysis

We used Horn's parallel analysis to determine the number of latent factors underlying our data. This process compares eigenvalues (representing the amount of variance captured by a latent factor) derived from the observed data to those derived from random datasets with the same size. Factors with eigenvalues more than 1 and more than their random counterparts were retained. A confirmatory factor analysis was then used to extract latent *g* scores from the manifest-level task scores (see section S1 for details on confounding factors).

Horn's parallel analysis found the eigenvalue of a single latent factor from the dataset was significantly higher than the eigenvalue of a single latent factor from a random dataset (Fig. S1a). Thus, we carried out a confirmatory factor analysis (CFA) with one specified general factor, which resulted in a model of good fit (Fig. S1b) with a low root mean square error of approximation (RMSEA = 0.01), a high comparative fit index (CFI = 0.98), and a high Tucker Lewis Index (TLI = 0.98). Statistical practices identify RMSEA values lower than 0.05, CFI values above 0.95, and TLI values above 0.95 as indicating good fit[17]. These results demonstrate that a single latent factor (*g*) underlies the shared individual differences variance across the administered cognitive tests.

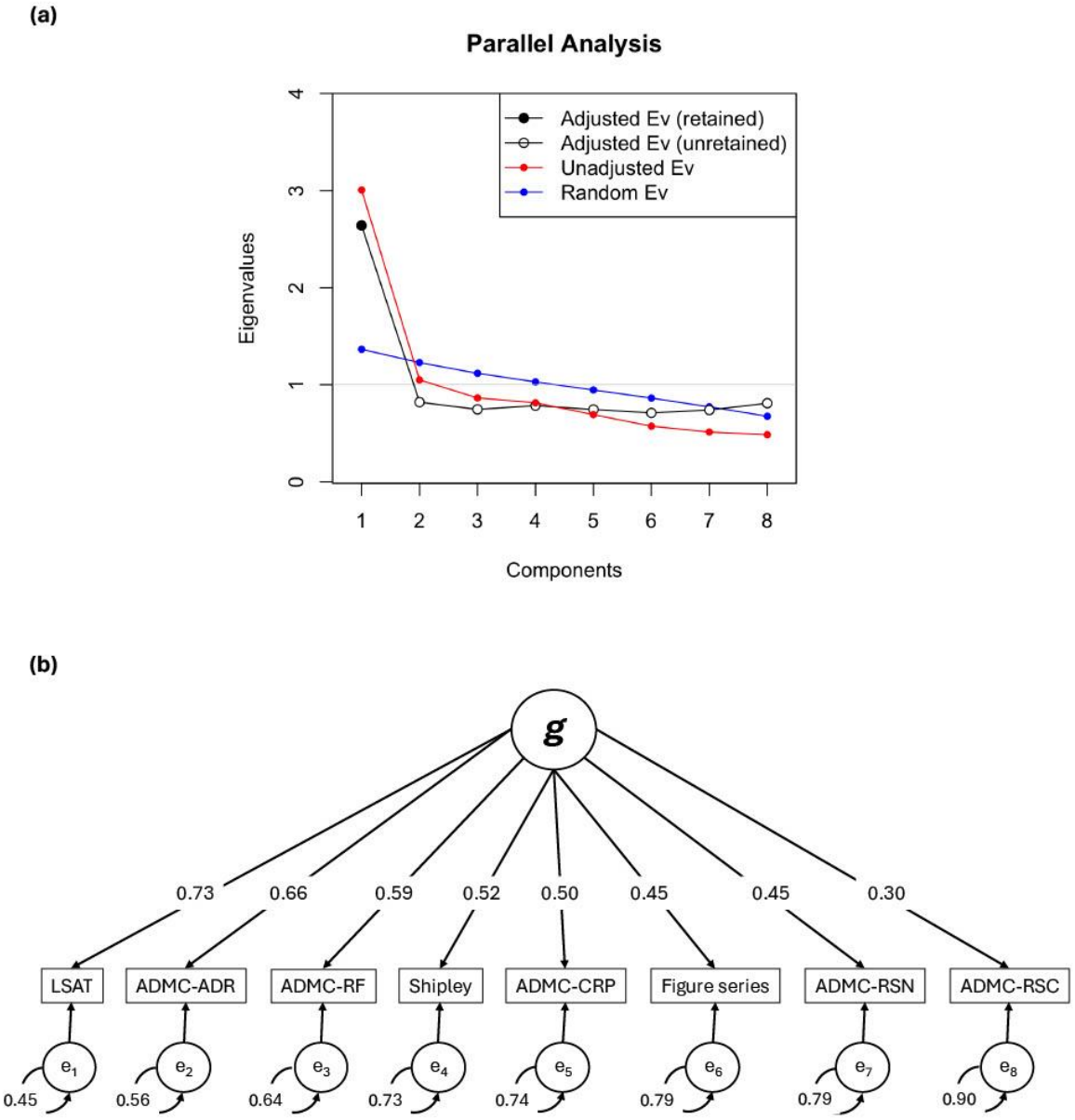

Figure S1. Results of the factor analysis used to generate subject *g* scores. **(a)** Plot of Horn's parallel analysis describing the eigenvalues for each component calculated from the observed data against the eigenvalues calculated from random data. The red line represents eigenvalues from the actual dataset. The black line represents eigenvalues from the actual dataset adjusted for sample size bias. The blue line represents the average eigenvalues from the random datasets. **(b)** A schematic of the confirmatory factor analysis. The rectangles identify the tests included. Loading values are overlaid on straight links. Error values are overlaid on circular links.

S3 Neuroimaging

Our analysis made use of anatomical, resting-state and diffusion-weighted scans collected during the INSIGHT1b study. Details of the procedures are included below.

S3.1. Imaging parameters

Scans were collected for all participants using a Siemens Magnetom 3 Tesla Trio scanner with a 32-channel head coil. Anatomical images were acquired using a multi-echo T1-weighted magnetization gradient echo sequence [0.9mm isotropic resolution, TR = 1900ms; TI = 900ms; TE = 2.32ms], with GRAPPA and an acceleration factor of 2. Resting-state images were acquired using a 10-min accelerated gradient echoplanar imaging (EPI) sequence [TR = 2000ms; TE = 30ms; FOV = 240mm; flip angle = 90°; 300 volumes; 1.9x.1.9x2.0mm voxel size; 56 slices with 10% slice gap]. Diffusion-weighted images were acquired using an accelerated gradient echoplanar imaging sequence [31 directions; b1 = 0s/mm^2; b2 = 1000s/mm^2; TR = 5000ms; TE = 100ms; FOV = 240mm; flip angle = 90°; 1.9x1.9x2.0mm voxel size; 72 slices].

S3.2. Processing pipelines

The high-resolution T1 MPRAGE images were brain extracted using Freesurfer.[18] Gray matter, white matter, and cerebrospinal fluid (CSF) voxels were delineated using Freesurfer's automatic segmentation procedure.

Resting-state images were preprocessed using FSL[19] and AFNI[20]. The images were: (1) motion-corrected; (2) brain extracted; (3) corrected for susceptibility-induced distortions and linearly registered to T1 space (2mm isotropic voxel resolution); (4) intensity-normalized; (5) smoothed using FSL's *susan* with a 4mm full-width-half-maximum kernel at 75% brightness threshold; and (6) linearly detrended using AFNI's *3dTproject*.

Diffusion-weighted images were preprocessed using FSL. These images were: (1) corrected for susceptibility-induced distortions; (2) brain extracted; and (3) corrected for eddy currents and movement. FSL's *dtifit* was then used to fit diffusion tensors from the processed images to obtain fractional anisotropy maps. These maps were used to register the Schaefer 200-7 atlas[21] in T1 space (200 nodes; 7 networks) to diffusion space. FSL's *bedpostx* was then used to fit probabilistic diffusion models. Finally, FSL's *probtrackx2* was run on the output of *bedpostx* using the Schaefer 200-7 atlas to define the cortical regions of interest. Five thousand streamlines

from each voxel in a cortical region were used as seeds. An exclusion CSF mask was implemented such that streamlines terminated if they crossed into CSF regions. The upper and lower triangles of each subject's structural connectome were averaged to form a symmetric matrix.

S3.3. Independent component analysis and network classification procedure

FSL's *melodic-ica* was applied to the preprocessed resting-state images to extract spatial co-activation patterns representative of signal (i.e., blood-oxygen-level-dependent signal) and noise (i.e., physiological artifacts). These spatial patterns were thresholded using probability maps supplied by the *melodic-ica* mixture model output. Voxels with probabilities less than chance of contributing to a co-activation pattern were zeroed out.

A modified version of Storti and colleagues' automatic resting-state networks selection algorithm[22] was then applied to classify co-activation patterns as either signal or noise. First, a Pearson's skewness index was calculated for each pattern. Patterns representing noise display a normal distribution centered around zero while patterns representing signal have more skewed distributions. Thus, we retained patterns with a skewness index above 0.1. The retained patterns were then masked with white matter and cerebrospinal fluid binary images derived from the *freesurfer* segmentation outputs. Voxels that overlapped with these masks were zeroed out. A spectral analysis was then performed on the functional time-series of voxels retaining some level of activation in each co-activation pattern. Because resting-state images are characterized by slow fluctuations of the blood-oxygen-level-dependent (BOLD) signal, only patterns with the vast majority ($\geq 70\%$) of their power in the 0.01-0.1 Hz range were retained.

The retained, cleaned patterns were then classified in terms of which ICN contributed the most to their observed functional activation values. A T1-registered Schaefer 200-7 atlas was applied to every signal-related pattern and functional activation values were averaged for each ICN. The ICN with the highest average functional activation for a given pattern was selected as representing its core network. If two or more patterns contained the same ICN as their core network, they were summed together. Average region-wise activation values were then calculated for each pattern, vectorized, and horizontally stacked to construct a functional activation matrix. The matrix contains seven columns that represent co-activation patterns, each with a single ICN at its core, and rows that represent the functional activation of cortical regions contributing to each pattern. It should be noted that while each column represents a distinct core ICN that contributed

the most to its observed functional activation values, the associated rows may also contain significant, albeit weaker, levels of functional activation in regions outside the core ICN, which represents between-network communications. Each structure-function circuit contains one of seven ICNs at its core, with additional between-network connections recovered from its underlying ICA spatial pattern that captured changes in regions' network affiliation.

S4. Connectome-based predictive modeling

S4.1. Cross-validation procedure

We used leave-one-out cross validation to predict out-of-sample g scores from the seven structure-function brain circuits across the whole brain. Leave-one-out cross-validation was employed to ensure maximal statistical power given the sample's much smaller size compared with the Human Connectome Project dataset.

Features were first transformed (see section S4.2 below). Then, connectome-based predictive modeling (CPM) was conducted based on the following steps: (1) the dataset was split into training and test sets; (2) connectivity features from each structure-function brain circuit in the training set were correlated with *g* scores (features with *p*-values above 0.01 were discarded); (3) significant connections were grouped into an upper *positive tail* (i.e., positively related to *g*) and a lower *negative tail* (i.e., negatively related to *g*); (4) connections within their respective categories were summed to generate both positive and negative summary statistics for each of the seven structure-function brain circuits resulting in fourteen independent variables; (5) these variables were used to fit a general linear model from the training set that generated predictions for the held-out test set.

S4.2. Feature transformation

Before running the analysis, all connectivity features were inversely transformed for easier evaluation. The structure-function connectivity strength distribution is similar to the distribution of connections found in structural connectomes. It has a ratio scale (i.e., contains an absolute zero) and is highly skewed such that a few extremely strong connections dominate the variance. Because we are interested in examining the role weak connections play in predicting individual differences in *g* scores, this kind of skewed distribution can be problematic. We address this issue

by boosting the variance associated with connections in the lower end of the distribution while preserving the monotonicity (i.e., rank order) of the connection strengths and their ratio scale. This is accomplished with a negative-inverse transformation (for considerations in the use of an inverse transformation see ref.[23]):

$$x_{transformed} = 1 + \left[-1/\left(1 + x_{original}\right)\right]$$

As a concrete example, Table S1 provides a set of numerical values and their transformed counterparts, showing that the transformation preserves both monotonicity and the ratio scale. As Figure S2 illustrates, the transformation boosts the variance within the lower end of the distribution. To determine the efficacy of this transformation, we repeated the whole-brain, connectome-based predictive model, but with features that did not undergo this transformation procedure (Fig. S3). Non-transformed strengths resulted in a lower correlation between observed and predicted *g* scores (r = 0.20), a lower coefficient of determination (R^2 = 0.01), and a higher normalized root mean square deviation (*nRMSD* = 0.99). This benefit is separate from the transformation's aid in our investigation of the role weak ties play in intelligence, as reported in the main text.

Original	Transformed
0.00	0.00
0.10	0.09
0.90	0.47
1.00	0.50
5.00	0.83
50.00	0.98
100.00	0.99

Table S1. Example transformation results. Values in the left column represent a sample set of numerical values. Values in the right column represent the transformed versions of the original values.

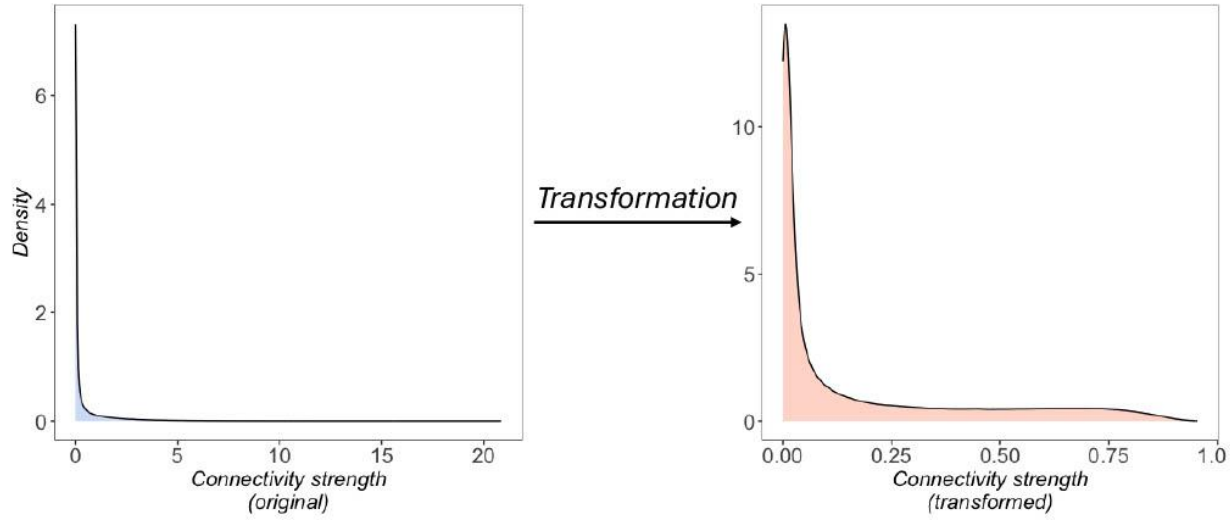

Figure S2. Visualization of the strength distributions of connectivity features before (left) and after the transformation (right). Density estimation with a Gaussian kernel was used to plot the distributions.

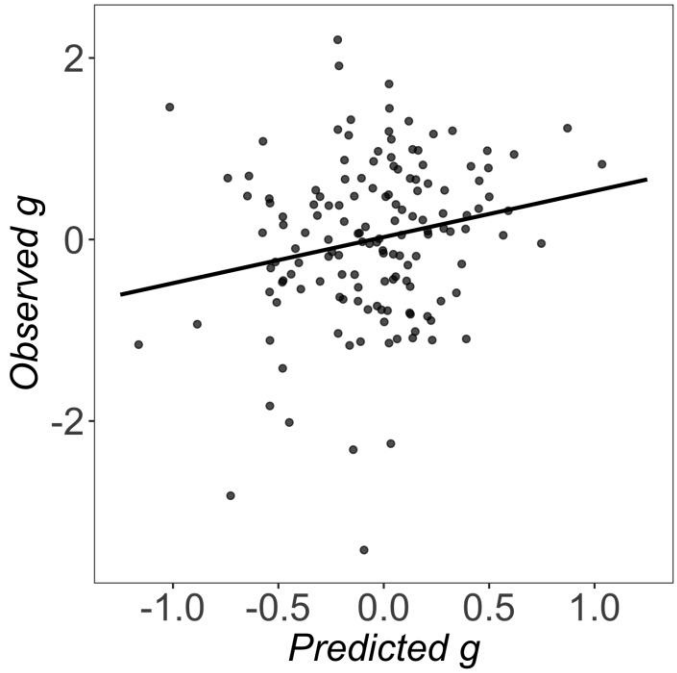

Figure S3. A whole-cortex CPM analysis with non-transformed, joint structure-function connections provides weaker results (r = 0.20; R^2 = 0.01; *nRMSD* = 0.99) compared to a CPM

analysis with transformed features (r = 0.37; R^2 = 0.15; *nRMSD* = 0.92). The graph depicts a scatterplot of predicted *g* scores compared to observed *g* scores from the analysis with non-transformed features.

S4.3. Predictive modeling results

Consistent with the predictions of NNT, a whole brain CPM incorporating all joint structure-function brain circuits reliably predicted out-of-sample *g* scores (Fig. S4a), explaining a significant proportion of the variance (R^2 = 0.15; P_{1000} = 0.007; Fig. S4b) and yielding a significant correlation between predicted and observed *g* scores (r = 0.37; P_{1000} = 0.007; Fig. S4c).

To assess the statistical significance of the CPM results, we conducted a permutation test with 1,000 random permutations, following established conventions[24,25]. This method creates a null distribution by randomly shuffling scores between subjects and running the predictive model in the same manner. Permutation testing is necessary to establish statistical significance in leave-one-out cross-validation because folds are not independent from one another, precluding the use of standard parametric tests. The observed *nRMSD* was significantly lower than the value obtained from a null distribution (*nRMSD* = 0.92; P_{1000} = 0.007; Fig. S4d).

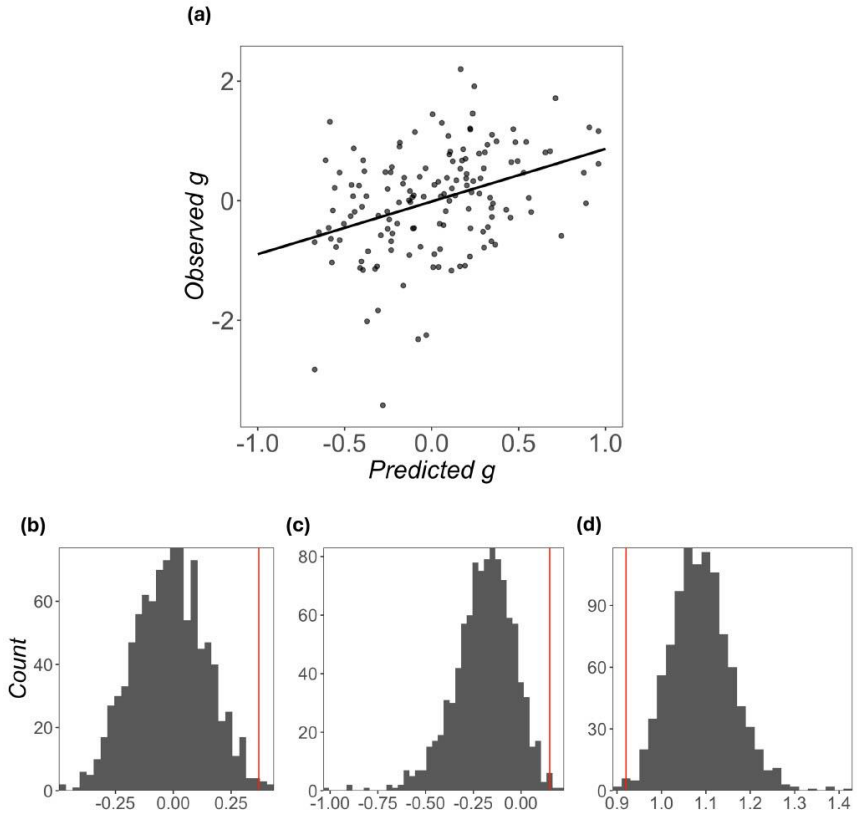

Figure S4. Joint structure-function brain circuits incorporating connections across the entire brain reliably predict general intelligence (r = 0.37; R^2 = 0.15; *nRMSD* = 0.92; n=145). **(a)** Scatterplot of predicted *g* scores compared to observed *g* scores. **(b)-(d)** Permutation tests of performance metrics with 1,000 randomly shuffled datasets were used to establish significance with respect to an empirically derived null distribution. Red lines represent statistical values from the whole-brain model. **(b)** Pearson correlation between observed and predicted values. **(c)** Coefficient of determination describing the proportion of variance explained. **(d)** The normalized root mean squared deviation indicating the average difference between observed and predicted *g* scores.

S5 Lesion analysis

To assess the predictive power of each brain circuit compared to our whole-brain model we adopted a lesion approach that predicts out-of-sample *g* scores from subsets of connectivity fea-

tures. This consisted of inclusion and exclusion brain circuit models. Inclusion models incorporated features from only one of the derived joint structure-function brain circuits in an iterative manner. This allowed us to test the independent predictive efficacy of each structure-function brain circuit compared to the whole-brain model. Conversely, exclusion models iteratively removed each structure-function brain circuit from the whole-brain model while keeping features from all others intact. This allowed us to see whether any brain circuit is crucial for the accurate prediction of *g* scores in the whole-brain model. Additionally, with respect to network allegiance, we characterized whether predictive connections derived from the lesion analyses primarily included those within or between ICNs. This was done by comparing the frequency of predictive connections from each brain circuit's core ICN with those representing all other ICNs.

S5.1 Lesion analysis results

Consistent with the predictions of NNT, inclusion analyses demonstrated that the independent predictive power of each structure-function brain circuit is lower than the whole-brain model (Fig. S5a). Nonetheless, circuits with the fronto-parietal (FPN), visual (VIS), salient attention (SAL), and limbic (LIM) ICNs at their core each demonstrated independent predictive efficacy (Fig. S5a). When structure-function circuits with these ICNs at their core were removed from the whole-brain model, performance decreased (Fig. S5b).

The lesion results demonstrated that not every structure-function brain circuit contributed to the prediction of *g*. Circuits with the somatomotor (SMN), dorsal attention (DAN), and default mode (DMN) ICNs at their core held no independent predictive power (Fig. S5a). When structure-function brain circuits with the SMN and DMN at their core were individually removed from the whole-brain model, the prediction of general intelligence improved (Fig. S5b). This suggests that the SMN and DMN may: (1) compete with or inhibit the functions underlying general intelligence; and/or (2) interact with other ICNs to produce a net positive contribution to *g*, rather than operating largely in isolation.

To evaluate these competing possibilities, we assessed whether predictive features underlying structure-function brain circuits that reliably predicted *g* (i.e., circuits with the FPN, VIS, SAL, or LIM networks at their core) were largely within- or between-network connections. This helped determine whether ICNs at the core of non-predictive circuits (e.g., SMN and DMN) were truly unrelated to *g* or influenced it through interactions with other ICNs. The vast majority of connections that survived the feature selection step for every predictive structure-function

brain circuit represented between-network links (78% of all predictive connections; Fig. S5c). Furthermore, the between-network predictive connections were predominantly mediated by the circuits with the FPN and DMN networks at their core (41%; Fig. S5c). This suggests that ICNs at the core of non-predictive structure-function circuits (e.g., the SMN and DMN) contribute to *g* through their between-network interactions. More broadly, the findings collectively support a globally integrated network architecture for intelligence – characterized by distributed and dynamic information processing, with between-network communication playing a critical role.

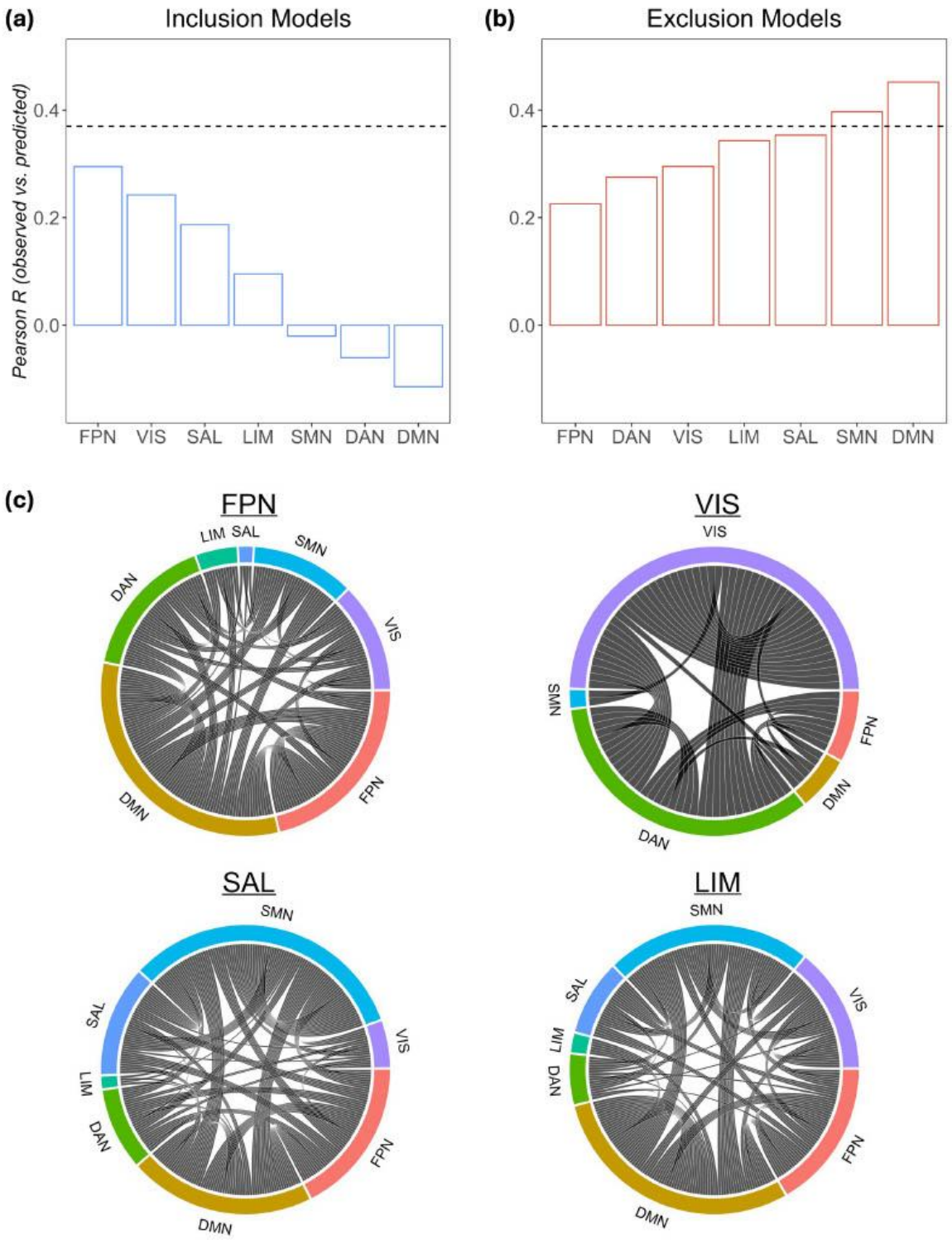

Figure S5. Lesion analyses examining the predictive performance of the individual structure-function brain circuits. The dotted line in graphs **a** and **b** represents the whole-brain model performance. Predictive structure-function brain circuits were selected based on whether they

held independent predictive power and contributed to the performance of the whole-brain model, as revealed by the lesion analyses. **(a)** Results from the inclusion analysis, where predictive performance was evaluated for connections originating in each joint structure-function brain circuit only. **(b)** Results from the exclusion analysis, where predictive performance was respectively evaluated for the whole-brain model with each circuit removed. **(c)** Chord diagrams illustrating the connection types (i.e., within- versus between-networks) that represent features underlying predictive joint structure-function brain circuits. Diagrams that are lighter in shade denote a greater number of predictive connections. Predictive connections are largely between different circuits (78%). Predictive between-network links are predominantly mediated by regions in the circuits with FPN and DMN networks at their cores (41%). Only connections positively correlated with *g* are shown in Figure S5c. See Figure S6 below for connections negatively correlated with *g*. FPN = Fronto-parietal Network; DMN = Default Mode Network; DAN = Dorsal Attention Network; LIM = Limbic Network; SAL = Salient Attention Network; SMN = Somatomotor Network; VIS = Visual Network.

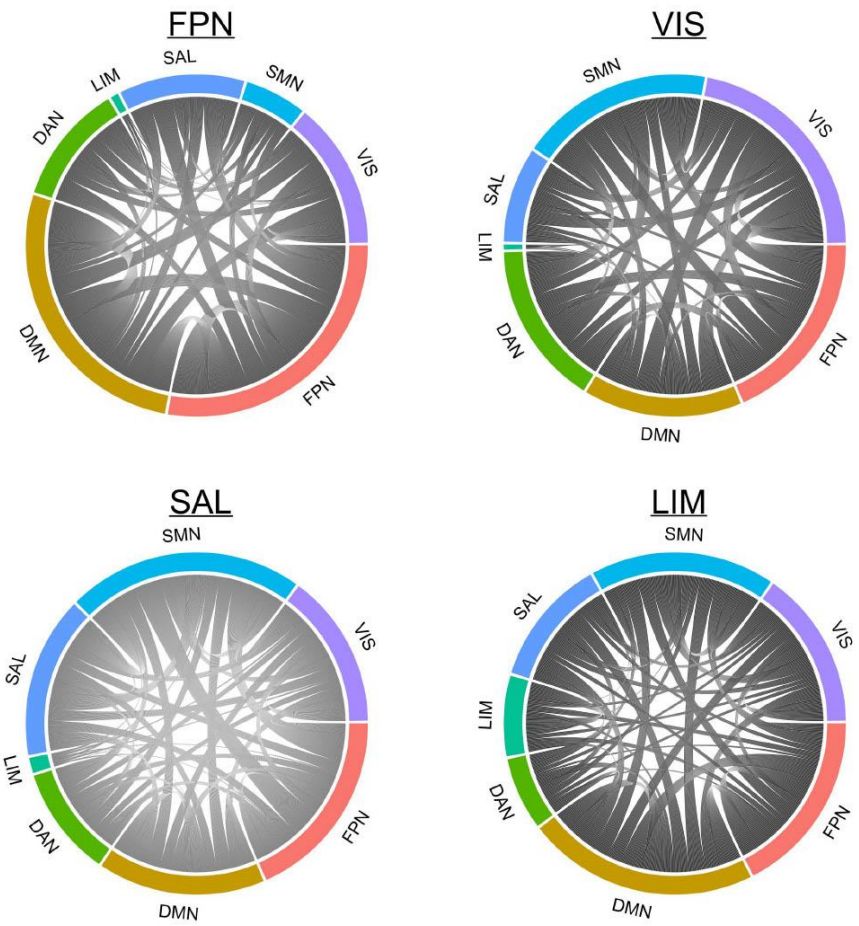

Figure S6. Chord diagrams illustrating the connection types (i.e., within- vs. between-networks) that represent negatively correlated features underlying predictive networks. Diagrams that are lighter in shade denote a greater number of predictive connections. FPN = Fronto-parietal Network; DMN = Default Mode Network; DAN = Dorsal Attention Network; LIM = Limbic Network; SAL = Salient Attention Network; SMN = Somatomotor Network; VIS = Visual Network.

S6 Topological characterization of *g*

With respect to network topology, we examined whether connections predictive of *g* were weak ties and representative of regions high in modal control. For these analyses, connections that survived the feature selection step were retained if they belonged to structure-function brain circuits that were both independent predictors of intelligence (revealed by the inclusion lesion analysis) and essential for whole-brain predictions (demonstrated by the exclusion lesion analysis).

S6.1. Weak ties analysis and results

The connections thus determined were concatenated across all folds and their strength averaged. The resulting distribution was compared to the distribution of strength of all connections (predictive and non-predictive) across subjects. Because the distributions are extremely skewed, the non-parametric Wilcoxon ranked-sum test with continuity correction was used to test this hypothesis. The mean strength of predictive connections was significantly lower than that of all connections from every structure-function brain circuit ($M_{predictive} = 0.01$; $SE_{predictive} = 0.02$; $M_{all} = 0.17$; $SE_{all} = 0.001$; $W = 66457470$; $p < 0.0001$), suggesting that weak connections play an outsize role in the prediction of *g*. As Figure S7a illustrates, this is not due to outliers but reflects the general distribution of predictive connections' strength.

We then determined whether such links are primarily long range. Prior research has shown that long-range connections are critical for forming short paths through global topologies. We therefore calculated the average shortest path length (ASPL) before and after predictive connections were removed to see if they primarily reflect long-range connections. We used the topology version of ASPL that averages the shortest number of direct connections that must be traversed between all pairwise regions. The ASPL is a global topological measure best calculated from connectomes that include all estimated links. No single joint structure-function brain circuit satisfies this criterion. We therefore used underestimation-corrected, whole-brain structural connectomes for this calculation. The joint structure-function model provides a matrix, *P*, whose values describe the extent to which underestimated structural connections were corrected. This matrix can be added to a structural connectome to create an underestimation-corrected, structural connectome. As such, predictive connections' underlying structural constituents were used for these analyses.

Distributions of ASPL generated before and after predictive connections were removed were inversely transformed to ensure normality. They were then compared to each other using a repeated-measures *t*-test. A permutation test was performed to ensure that differences in the brain's global topology were not simply due to the number of connections being removed but rather to the removal of the specific predictive connections themselves. To produce the null distribution for the permutation test, we followed the same steps as before but instead of removing predictive connections, we removed an equal number of randomly chosen ones. This process was repeated one thousand times to ensure reliability.

The Lilliefors normality test indicated that the inverse distributions of ASPL calculated before and after predictive connections were removed slightly differed from a normal distribution (D_{before} = 0.08; p_{before} = 0.04; D_{after} = 0.08; p_{after} = 0.04). When predictive connections were removed from the whole-brain connectome, the inverse ASPL decreased (Fig. S7b). Given the slight deviation from normality of the distributions, a nonparametric permutation test confirmed the significance of this change was due to the removal of predictive connections and not merely the number of links removed (M_{diff} = -0.03; p_{1000} = 0.001; Fig. S7c). This suggests that the structural constituents underlying structure-function connections important for predicting *g* form short path lengths between distant regions that are critical for efficient, system-wide communication. Figure S7d illustrates this point visually, with structure-function connections predictive of *g* traversing long distances spanning different brain networks, lobes, and hemispheres (see section S6.3 below for similar graphs depicting all predictive brain circuits). Taken together, the findings validate the predictions of NNT, demonstrating that general intelligence depends on weak, long-range connections.

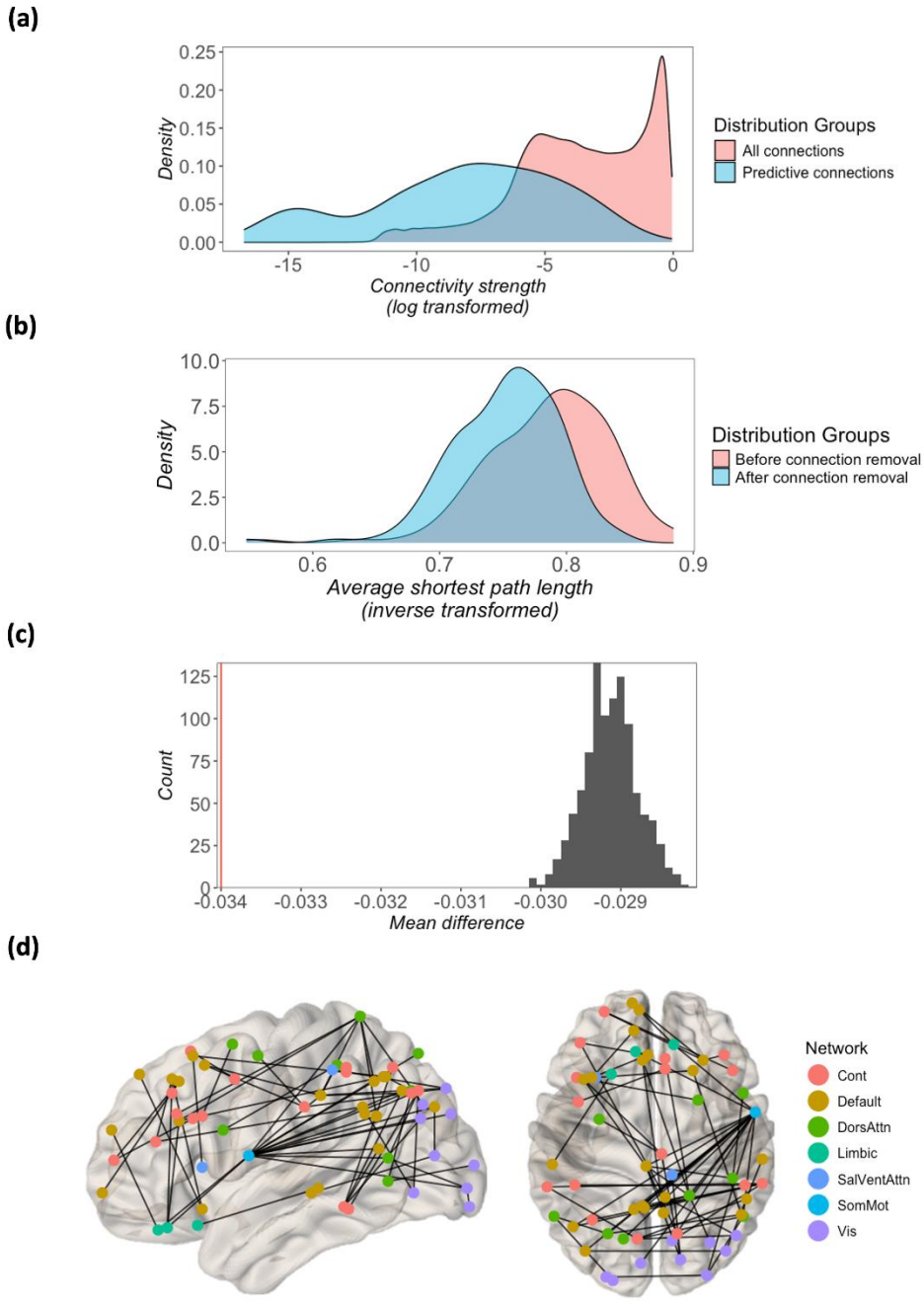

Figure S7. Assessment of weak ties within the set of predictive connections. **(a)** Comparison of distributions from predictive (blue) and all (red) connections using density estimation graphs with a Gaussian kernel. Connectivity strengths were log-transformed for visualization. **(b)** Distributions of inverse average shortest path length calculated before (red) and after (blue) predictive connections were removed from the underestimation-corrected, whole-brain structural connectome. Density estimation with a Gaussian kernel was used for plotting. **(c)** Permutation

test (with 1,000 iterations) of the mean difference in inverse average shortest before and after random connections were removed from the whole-brain connectome. The red line represents the statistical value from the actual dataset. **(d)** Predictive connections positively associated with *g* from the joint structure-function brain circuit with the fronto-parietal network at its core. See section S6.3 for images depicting the other predictive structure-function brain circuits.

S6.2 Modal control analysis and results

To investigate whether predictive connections are located where they can uniquely orchestrate global network activity, we calculated modal control values. Given modal control is a structural mechanism, underestimation-corrected structural connectomes were also used for these analyses. Predictive connections were separated by the primary structure-function brain circuit they belonged to and whether they related positively or negatively to *g*, resulting in two sets for each predictive brain circuit. The connections in these sets were then used to calculate modal control metrics (see ref.[26] for calculation details). The modal control metrics were categorized by positive or negative association with *g* and whether they came from a brain circuit mainly mediating control (FPN and SAL) or non-control (VIS and LIM) processes. Summing across modal control metrics in each process category resulted in four summary statistics, representing the summation of control or non-control nodes, positively versus negatively correlated with *g*.

The nested data for the multi-level modeling framework was structured in two levels; Level 1 (association type, i.e., positive or negative), and Level 2 (individuals). Separate models were fit by process category (i.e., control or non-control processes) to predict the summary metrics from *g* scores while controlling for association type.

A variation of Levene's test of equal variances was applied to examine the reliability of results in terms of homoscedasticity. This method extracts the residuals of the model, squares their absolute values, and then performs an ANOVA on the squared residuals. A non-significant *F* statistic suggests that the variance of the residuals is statistically equal across subjects. Log-likelihood ratios were used to evaluate the main effects. Control and non-control models both passed the check for homogeneity of variance (FPN and SAL: $F(144, 145) = 0.93$; $p = 0.67$; VIS and LIM: $F(144, 145) = 1.2$; $p = 0.13$).

Results showed that individuals with higher *g* scores exhibited greater modal control in regions supporting predictive connections from structure-function brain circuits with the FPN

and SAL at their core (FPN and SAL; $\beta = 0.08$, $L_{ratio} = 5.96$, $p = 0.01$; Fig. S8a). Furthermore, nodes supporting connections positively correlated with *g* exhibited higher levels of modal control than nodes supporting negatively correlated connections in these control circuits ($\beta = 1.65$, $L_{ratio} = 272.50$, $p < 0.0001$; Fig. S8a). The summary metrics generated from non-control networks (i.e., VIS and LIM) did not significantly relate to *g* ($\beta = -0.01$, $L_{ratio} = 0.09$, $p = 0.77$; Fig. S8b). This pattern of findings supports the predictions of NNT, demonstrating that general intelligence depends on the brain's capacity to engage modal control mechanisms that orchestrate global network activity.

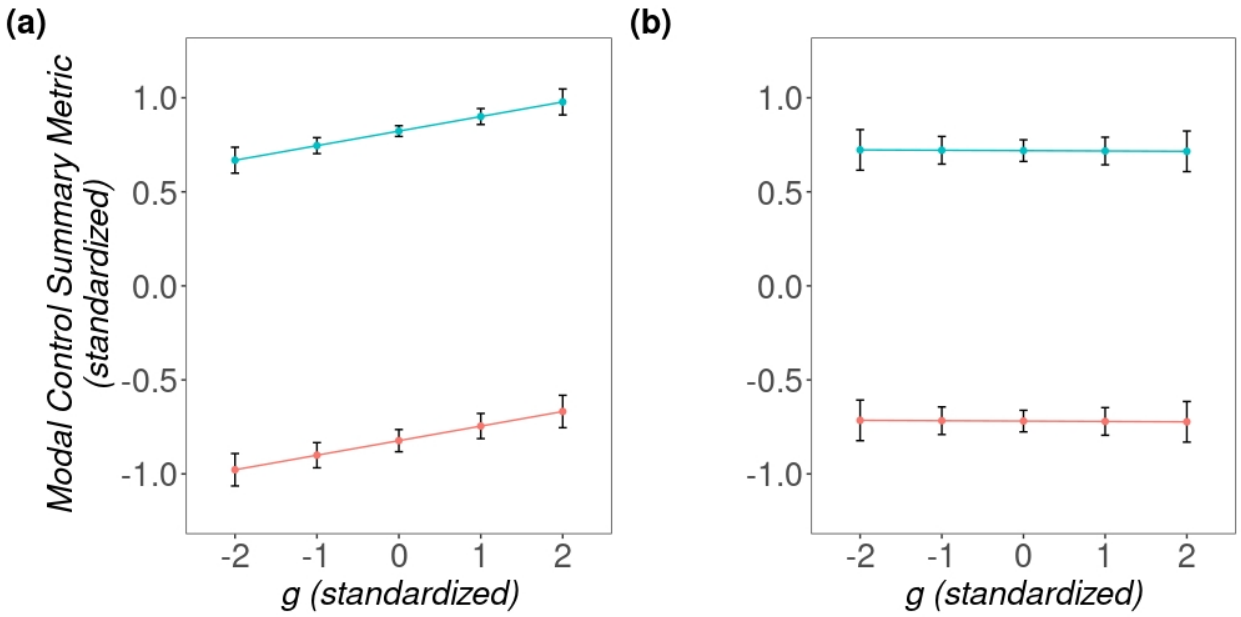

Figure S8. Group-level modal control effects based on multi-level modeling. **(a)** Predicted modal control summary values for fronto-parietal (FPN) and salient attention (SAL) brain circuits for different standardized *g* scores. **(b)** Predicted modal control summary values for non-control brain circuits (VIS and LIM) across different standardized *g* scores. Blue lines represent modal control values generated from connections positively correlated with *g*, red lines for negatively associated ones. Error bars represent 95% confidence intervals for the predicted values.

S6.3 Structure-function connections from predictive circuits

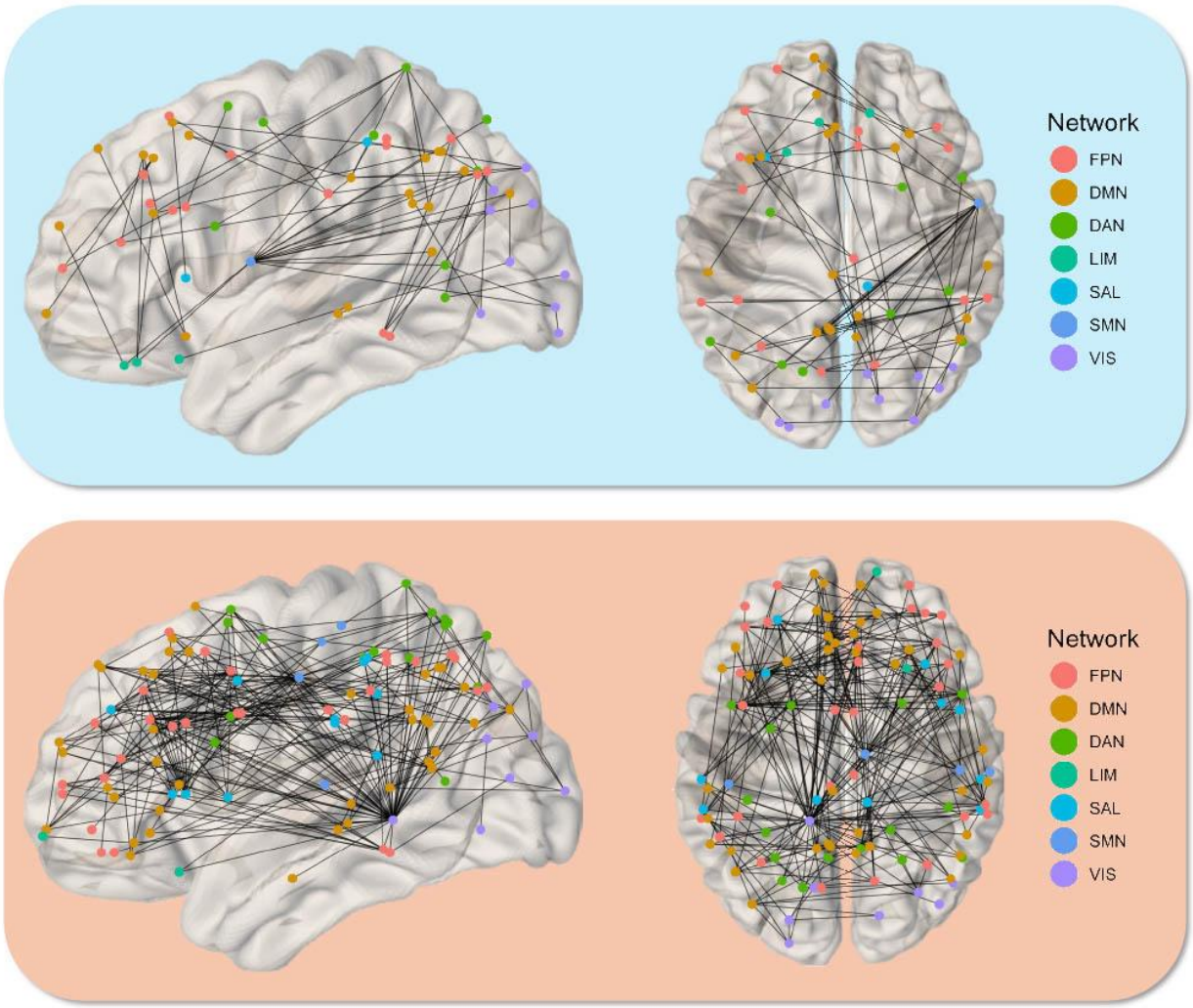

Figure S9. Predictive connections from the fronto-parietal circuit. Connections positively correlated with *g* are shown in the light blue panel. Connections negatively correlated with *g* are shown in the red panel. Note the length of most predictive connections.

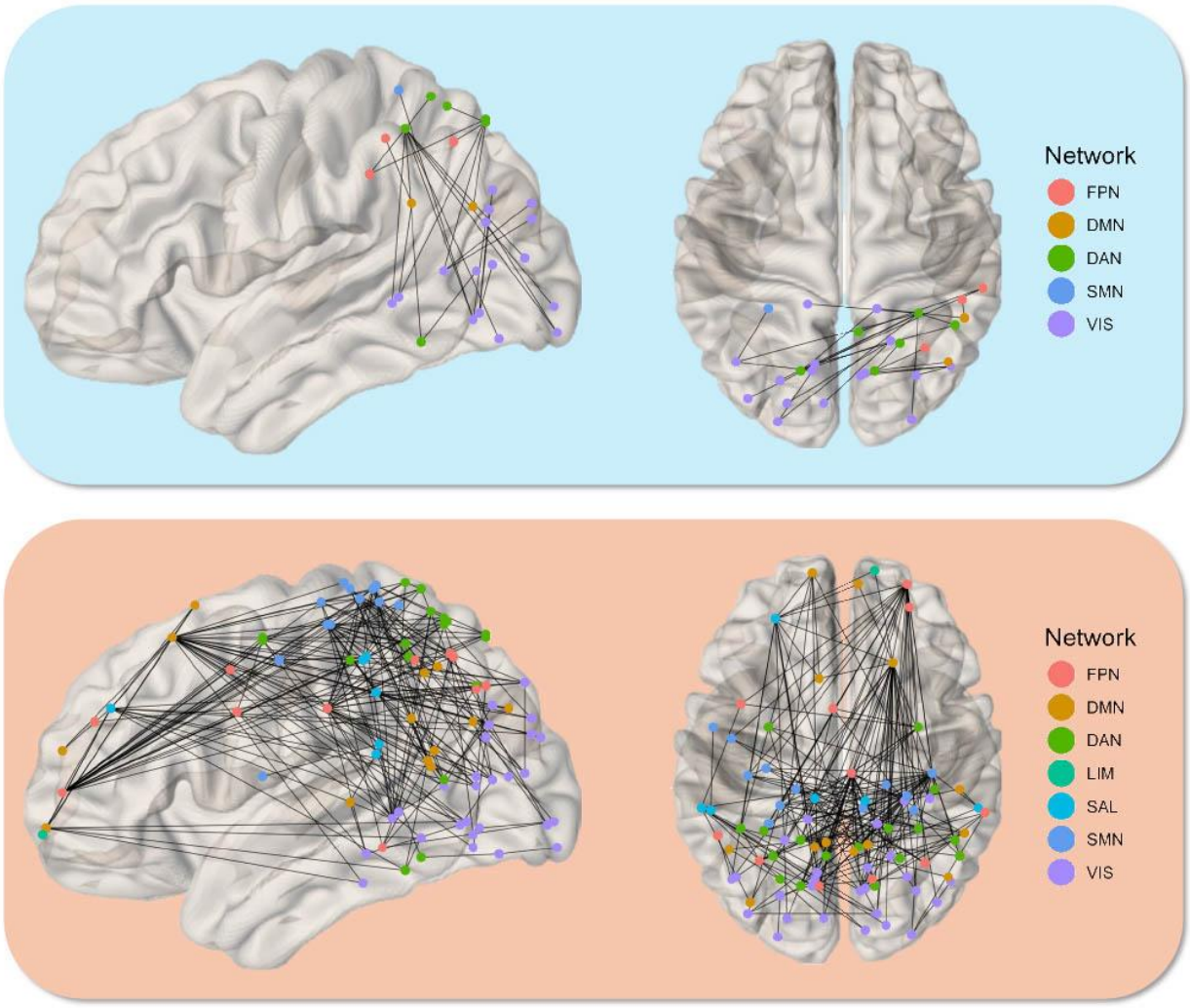

Figure S10. Predictive connections from the Visual circuit. Connections positively correlated with *g* are shown in the blue panel. Connections negatively correlated with *g* are shown in the red panel.

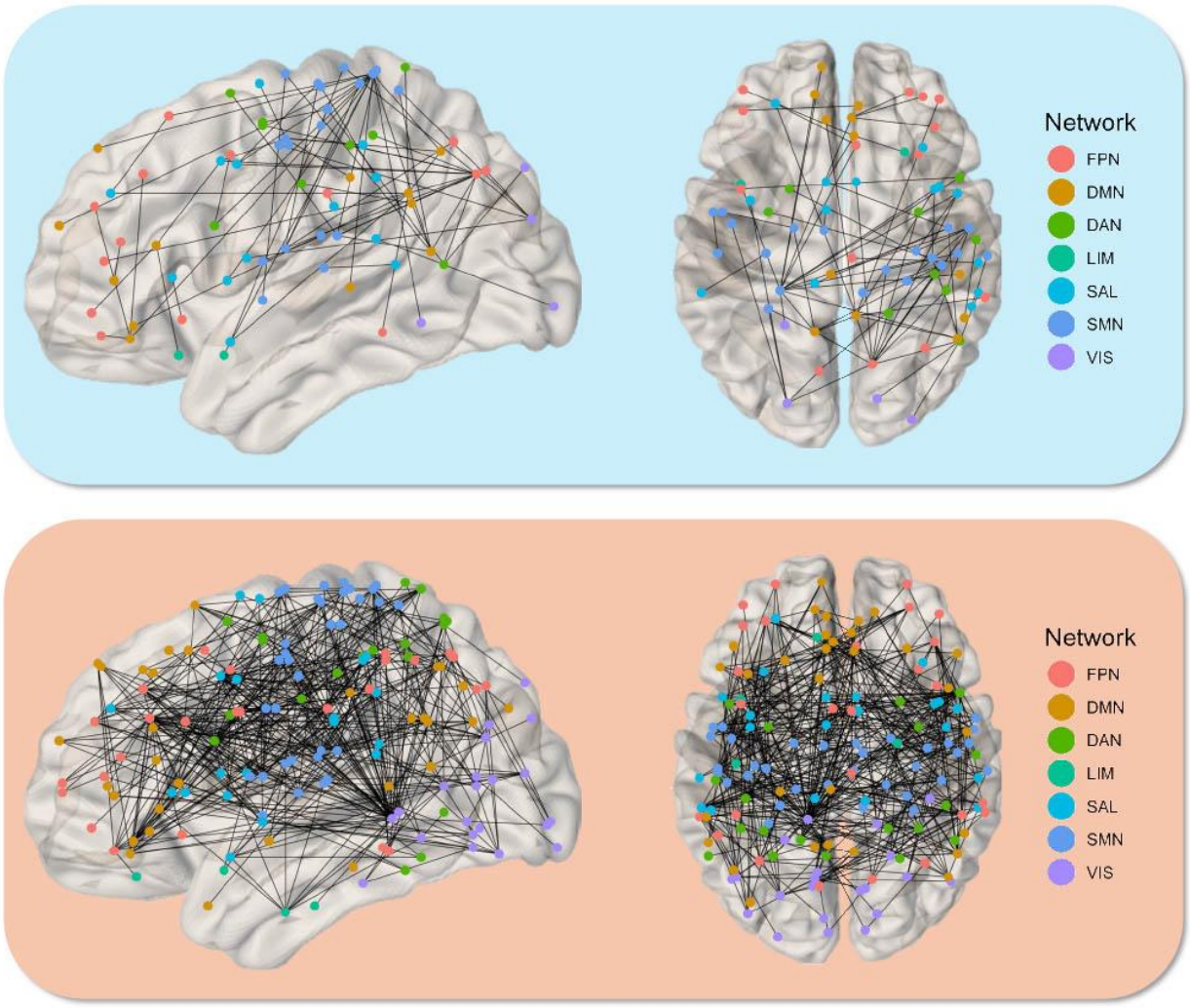

Figure S11. Predictive connections from the Salient Attention circuit. Connections positively correlated with *g* are shown in the blue panel. Connections negatively correlated with *g* are shown in the red panel.

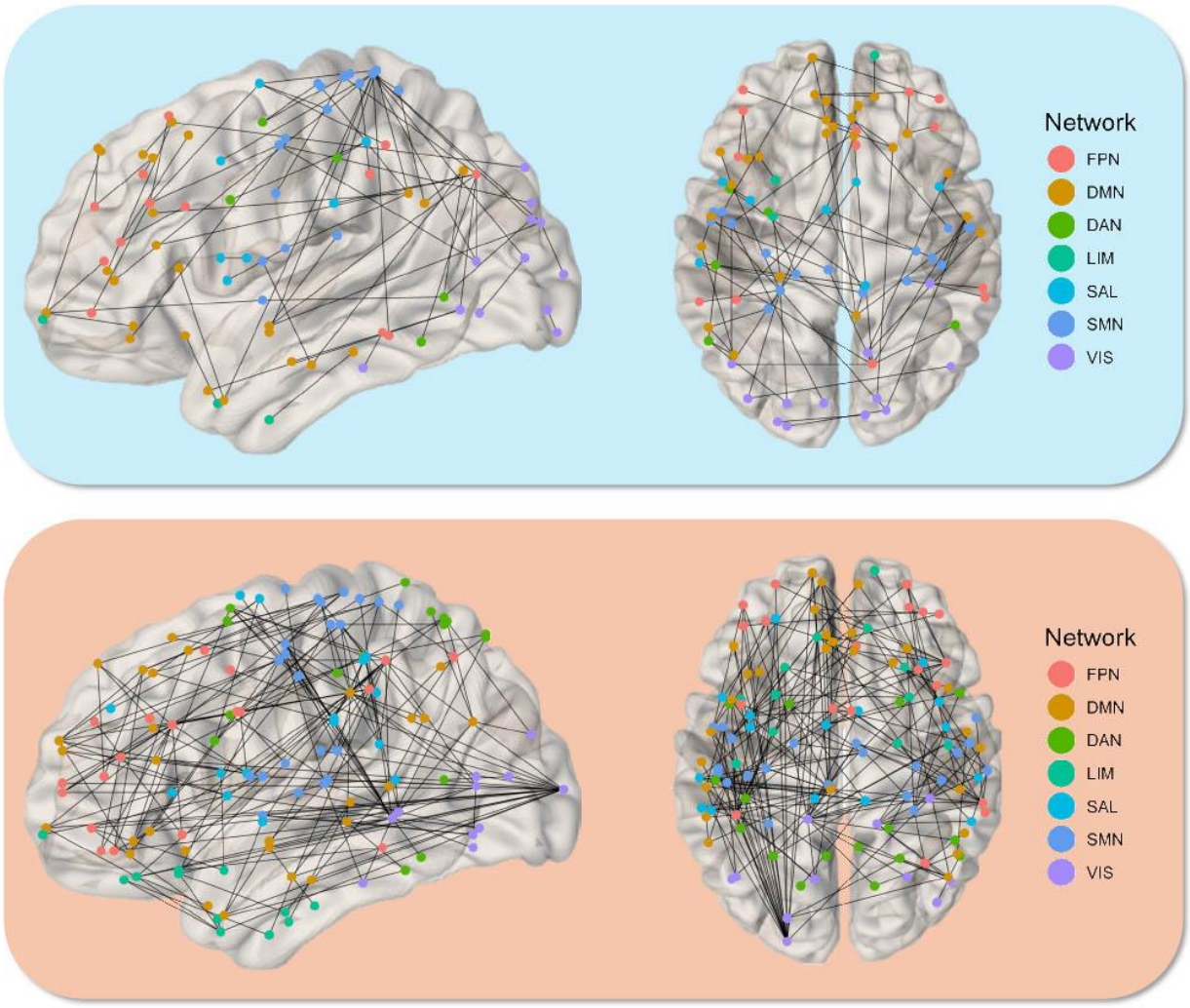

Figure S12. Predictive connections from the Limbic circuit. Connections positively correlated with *g* are shown in the blue panel. Connections negatively correlated with *g* are shown in the red panel.

S7 Small-worldness and *g*

We investigated whether *g* relies on the brain's global, small-world topology. Like average shortest path length and modal control analyses, we calculated small-worldness from underestimation-corrected, whole-brain structural connectomes given its focus on the brain's global topology. We employed Telesford and colleagues'[27] improvements upon the approach proposed by Watts and Strogatz[28,29] to extract small-world metrics. Values close to 0 indicate small world topologies,

values closer to -1 indicate a deviation towards a more regular network, and values closer to 1 indicate a deviation towards a more random network (see below S7.1 for more details). To further examine the relationship between *g* and specific elements of a small-world topology, we also report average shortest path length and average local clustering coefficient. Pearson correlation coefficients were generated with associated *p*-values to assess the ability of the various attributes to predict *g*.

S7.1 The measure and its distribution

A small-world network is somewhere between a regular network and a random network. This leads to a topology that exhibits both a high degree of local clustering (exemplified in regular networks) and short path lengths (exemplified in random networks). Simulation studies have shown that a network can evolve from a regular topology to a small-world topology, and finally to a random topology as a function of the probability of randomly rewiring its connections[28,30]. As the probability of rewiring the network's connections increases, there is a critical phase where the network begins to exhibit short, global path lengths while maintaining its high degree of local clustering. However, once this rewiring probability becomes too high, local clustering begins to break down and the network starts to exhibit a random topology. Early small-world metrics[29] measured this behavior on a linear scale, with higher scores signifying greater small-worldness and lower scores lesser small-worldness. Thus construed, the scale does not identify the direction in which a network may deviate from a small-world topology (i.e., whether it is towards a more regular or a more random network). More informative alternatives have been proposed. We use one such metric[27] that exists on a scale from -1 to 1, where values close to 0 represent a small-world network, more positive values indicate deviation towards a more random network, and more negative values indicate deviation towards a more regular network. While more helpful for characterizing networks, this nonlinear relationship can potentially make it more difficult to examine linear relationships with behavior. However, as individuals in our dataset deviated in only one direction, this issue was sidestepped. Figure S13 demonstrates that the only deviation in the dataset away from a small world topology is one towards a more random network structure. Thus, we were able to linearly assess the relationship between *g* and the brain's small-world topology while providing greater information about the nature of deviations from it in individuals exhibiting lower *g* scores.

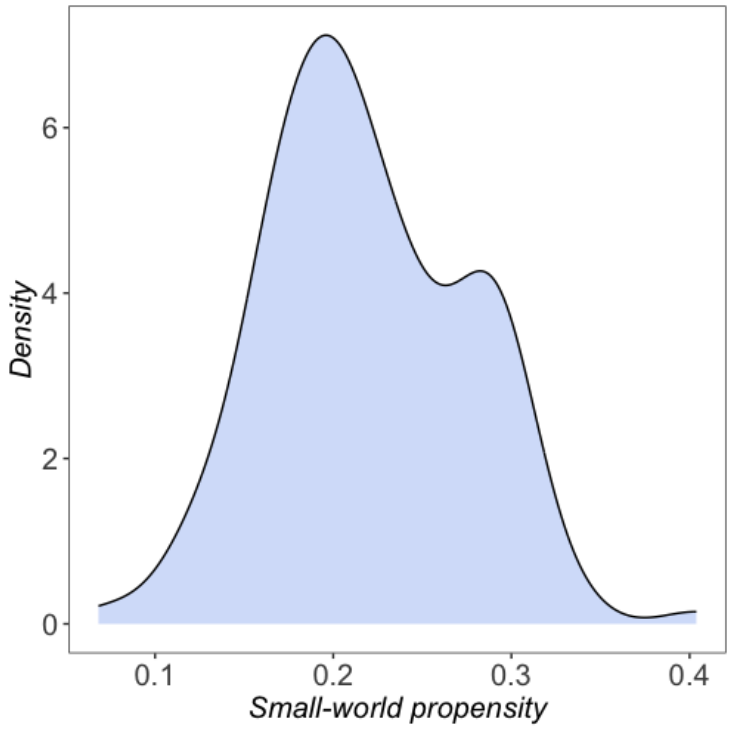

Figure S13. Distribution of small-world propensity values (square root transformed) calculated using the Telesford method from underestimation-corrected, whole-brain structural connectomes. Density estimation with a Gaussian kernel was used for plotting.

S7.2 Small-worldness and *g* results

Small-worldness values were square root transformed to ensure normality. The Lilliefors normality test indicated this transformed distribution did not significantly differ from a normal distribution ($D = 0.07$; $p = 0.08$). Values close to 0 denote greater small-worldness, whereas values closer to 1 indicate a deviation towards a more random network (see previous section S7.1 for details about the distribution of small-world values). As predicted, individuals with higher *g* scores exhibited greater small-worldness than individuals with lower *g* scores ($r = -0.20$; $t(143) = -2.48$; $p = 0.01$; Fig. S14a). Complementary analyses examining the topological properties that underlie small-worldness (i.e., average shortest path length and average local clustering) provided additional support for this relationship. Individuals with higher *g* scores exhibited higher inverse path length values ($r = 0.21$; $t(143) = 2.52$; $p = 0.01$; Fig. S14b), thereby showing shorter average path lengths. The Lilliefors normality test indicated this distribution did not significantly differ from a normal distribution ($D = 0.07$; $p = 0.06$). These individuals also demonstrated larger average lo-

cal clustering coefficients (r = 0.21; $t(143)$ = 2.52; p = 0.01; Fig. S14c). Again, a normality test indicated no significant deviation from a normal distribution (D = 0.07; p = 0.08). Together, the results indicated enhanced local clustering and better global integration in the structural connectomes of individuals with higher *g* scores. The observed findings support the NNT framework, providing evidence that intelligence emerges from the brain's small-world organization.

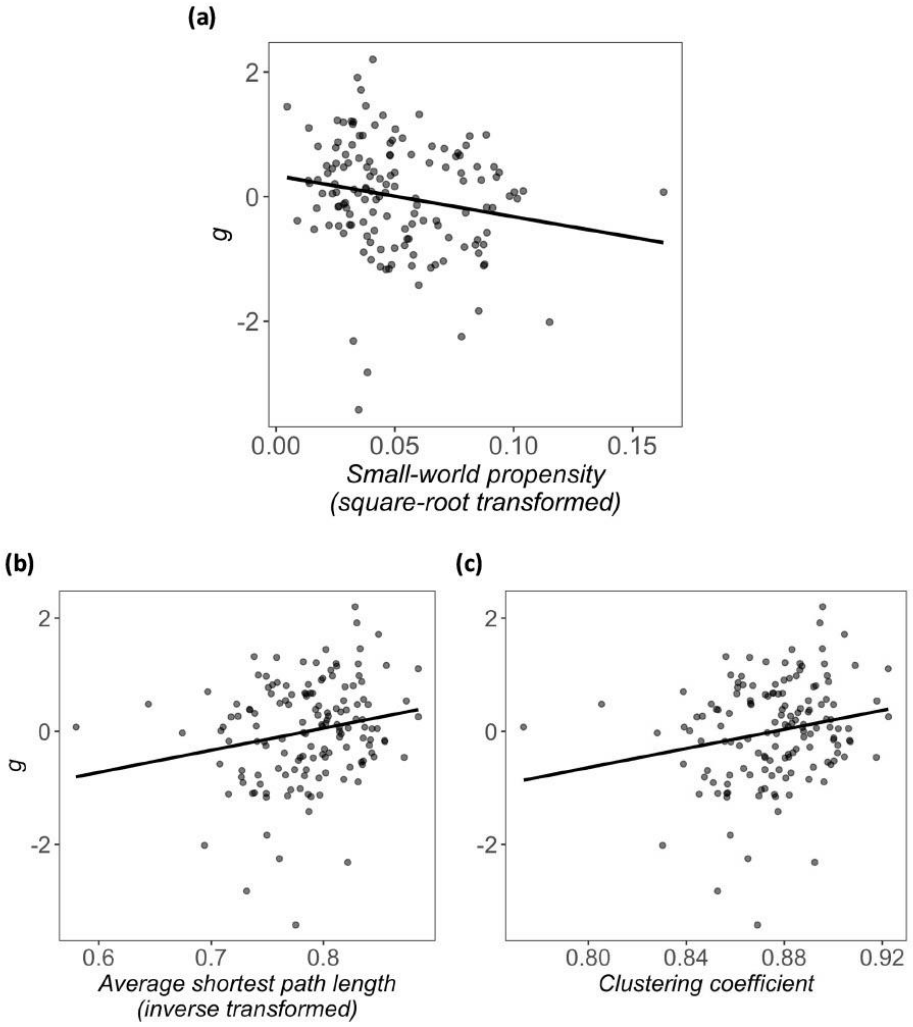

Figure S14. Correlations between *g* and the small-world organization of the underestimation-corrected, whole-brain structural connectomes. **(a)** Scatter plot of *g* scores against small-world propensity values (square-root transformed) showing a negative correlation (r = -0.21; p = 0.01). Values above zero denote deviation away from a small-world architecture towards a more random network. **(b)** Scatter plot of *g* scores against average shortest path lengths (inverse-

transformed) showing a positive correlation ($r = 0.22$; $p = 0.008$). Higher values denote shorter average path lengths. **(c)** Scatter plot of *g* scores against local clustering coefficient showing a positive correlation ($r = 0.23$; $p = 0.005$). Higher values denote greater local clustering.

Supplementary References

1. Hudson, R. Explicating Exact versus Conceptual Replication. *Erkenntnis* **88**, 2493–2514 (2023).
2. Daugherty, A. M. *et al.* Individual differences in the neurobiology of fluid intelligence predict responsiveness to training: Evidence from a comprehensive cognitive, mindfulness meditation, and aerobic exercise intervention. *Trends Neurosci. Educ.* **18**, 100123 (2020).
3. Zwilling, C. E. *et al.* Enhanced decision-making through multimodal training. *Npj Sci. Learn.* **4**, 11 (2019).
4. Wilcox, R. R. & Barbey, A. K. Connectome-based predictive modeling of fluid intelligence: evidence for a global system of functionally integrated brain networks. *Cereb. Cortex* **33**, 10322–10331 (2023).
5. Anderson, E. D. & Barbey, A. K. Investigating cognitive neuroscience theories of human intelligence: A connectome-based predictive modeling approach. *Hum. Brain Mapp.* **44**, 1647–1665 (2023).
6. Thomas, S., Reading, J. & Shephard, R. J. Revision of the Physical Activity Readiness Questionnaire (PAR-Q). *Can. J. Sport Sci. J. Can. Sci. Sport* **17**, 338–345 (1992).
7. Thomas Yeo, B. T. *et al.* The organization of the human cerebral cortex estimated by intrinsic functional connectivity. *J. Neurophysiol.* **106**, 1125–1165 (2011).
8. Mackey, A. P., Singley, A. T. M., Wendelken, C. & Bunge, S. A. Characterizing Behavioral and Brain Changes Associated with Practicing Reasoning Skills. *PLOS ONE* **10**, e0137627 (2015).
9. Kyllonen, P. *et al.* General fluid/inductive reasoning battery for a high-ability population. *Behav. Res. Methods* **51**, 507–522 (2019).
10. Kaya, F., Delen, E. & Bulut, O. Test review: Shipley-2 manual. *J. Psychoeduc. Assess.* **30**, 593–597 (2012).

11. Bruine de Bruin, W., Parker, A. M. & Fischhoff, B. Individual differences in adult decision-making competence. *J. Pers. Soc. Psychol.* **92**, 938–956 (2007).
12. Kaufman, S. B., DeYoung, C. G., Reis, D. L. & Gray, J. R. General intelligence predicts reasoning ability even for evolutionarily familiar content. *Intelligence* **39**, 311–322 (2011).
13. McGrew, K. S. CHC theory and the human cognitive abilities project: Standing on the shoulders of the giants of psychometric intelligence research. *Intelligence* **37**, 1–10 (2009).
14. Blacksmith, N., Behrend, T. S., Dalal, R. S. & Hayes, T. L. General mental ability and decision-making competence: Theoretically distinct but empirically redundant. *Personal. Individ. Differ.* **138**, 305–311 (2019).
15. Bruine de Bruin, W., Parker, A. M. & Fischhoff, B. Decision-Making Competence: More Than Intelligence? *Curr. Dir. Psychol. Sci.* **29**, 186–192 (2020).
16. Román, F. J. *et al.* Cognitive and neural architecture of decision making competence. *NeuroImage* **199**, 172–183 (2019).
17. Hu, L. & Bentler, P. M. Cutoff criteria for fit indexes in covariance structure analysis: Conventional criteria versus new alternatives. *Struct. Equ. Model. Multidiscip. J.* **6**, 1–55 (1999).
18. Fischl, B. FreeSurfer. *NeuroImage* **62**, 774–781 (2012).
19. Jenkinson, M., Beckmann, C. F., Behrens, T. E. J., Woolrich, M. W. & Smith, S. M. FSL. *NeuroImage* **62**, 782–790 (2012).
20. Cox, R. W. AFNI: Software for Analysis and Visualization of Functional Magnetic Resonance Neuroimages. *Comput. Biomed. Res.* **29**, 162–173 (1996).
21. Schaefer, A. *et al.* Local-Global Parcellation of the Human Cerebral Cortex from Intrinsic Functional Connectivity MRI. *Cereb. Cortex* **28**, 3095–3114 (2018).
22. Storti, S. F. *et al.* Automatic selection of resting-state networks with functional magnetic resonance imaging. *Front. Neurosci.* **7**, (2013).
23. Osborne, J. Notes on the use of data transformations. *Pract. Assess. Res. Eval.* **8**, 6 (2002).
24. Shen, X. *et al.* Using connectome-based predictive modeling to predict individual behavior from brain connectivity. *Nat. Protoc.* **12**, 506–518 (2017).
25. Dubois, J., Galdi, P., Paul, L. K. & Adolphs, R. A distributed brain network predicts general intelligence from resting-state human neuroimaging data. *Philos. Trans. R. Soc. B Biol. Sci.* **373**, 20170284 (2018).

26. Karrer, T. M. *et al.* A practical guide to methodological considerations in the controllability of structural brain networks. *J. Neural Eng.* **17**, 026031 (2020).

27. Telesford, Q. K., Joyce, K. E., Hayasaka, S., Burdette, J. H. & Laurienti, P. J. The Ubiquity of Small-World Networks. *Brain Connect.* **1**, 367–375 (2011).

28. Watts, D. J. & Strogatz, S. H. Collective dynamics of 'small-world' networks. *Nature* **393**, 440–442 (1998).

29. Humphries, M. D. & Gurney, K. Network 'Small-World-Ness': A Quantitative Method for Determining Canonical Network Equivalence. *PLOS ONE* **3**, e0002051 (2008).

30. Bassett, D. S. & Bullmore, E. Small-World Brain Networks. *The Neuroscientist* **12**, 512–523 (2006).